

High optical transmittance of aluminum ultrathin film with hexagonal nanohole arrays as transparent electrode

Qing Guo Du,^{1,*} Weisheng Yue,² Zhihong Wang,³ Wah Tung Lau,¹ Hengjiang Ren,⁴ and Er-Ping Li⁵

¹Department of Physics, University of Toronto, 60 St. George St., Toronto, Ontario, M5S 1A7, Canada

²National Graphene Institute, University of Manchester, Oxford Road, Manchester M13 9PL, UK

³Advanced Nanofabrication Core Lab, King Abdullah University of Science and Technology, Thuwal 23955-6900, Saudi Arabia

⁴Electrical Engineering, California Institute of Technology, 1200 E. California Blvd, Pasadena, CA 91125, USA

⁵Department of Information Science & Electronic Engineering, Zhejiang University, Hangzhou 310027, Zhejiang, China

*duqi0001@e.ntu.edu.sg

Abstract: We fabricate samples of aluminum ultrathin films with hexagonal nanohole arrays and characterize the transmission performance. High optical transmittance larger than 60% over a broad wavelength range from 430 nm to 750 nm is attained experimentally. The Fano-type resonance of the excited surface plasmon polaritons and the directly transmitted light attribute to both of the broadband transmission enhancement and the transmission suppression dips.

©2016 Optical Society of America

OCIS codes: (310.6628) Subwavelength structures, nanostructures; (240.6680) Surface plasmons; (130.0250) Optoelectronics.

References and links

1. Z. Chen, B. Cotterell, W. Wang, E. Guenther, and S.-J. Chua, "A mechanical assessment of flexible optoelectronic devices," *Thin Solid Films* **394**(1-2), 201–205 (2001).
2. H.-K. Kim, D.-G. Kim, K.-S. Lee, M.-S. Huh, S. H. Jeong, K. I. Kim, and T.-Y. Seong, "Plasma damage-free sputtering of indium tin oxide cathode layers for top-emitting organic light-emitting diodes," *Appl. Phys. Lett.* **86**(18), 183503 (2005).
3. B. O'Connor, C. Haughn, K.-H. An, K. P. Pipe, and M. Shtein, "Transparent and conductive electrodes based on unpatterned, thin metal films," *Appl. Phys. Lett.* **93**(22), 223304 (2008).
4. J.-F. Salinas, H.-L. Yip, C.-C. Chueh, C.-Z. Li, J.-L. Maldonado, and A. K. Y. Jen, "Optical design of transparent thin metal electrodes to enhance in-coupling and trapping of light in flexible polymer solar cells," *Adv. Mater.* **24**(47), 6362–6367 (2012).
5. S. De, T. M. Higgins, P. E. Lyons, E. M. Doherty, P. N. Nirmalraj, W. J. Blau, J. J. Boland, and J. N. Coleman, "Silver nanowire networks as flexible, transparent, conducting films: extremely high DC to optical conductivity ratios," *ACS Nano* **3**(7), 1767–1774 (2009).
6. J.-Y. Lee, S. T. Connor, Y. Cui, and P. Peumans, "Solution-processed metal nanowire mesh transparent electrodes," *Nano Lett.* **8**(2), 689–692 (2008).
7. L. Hu, H. S. Kim, J.-Y. Lee, P. Peumans, and Y. Cui, "Scalable coating and properties of transparent, flexible, silver nanowire electrodes," *ACS Nano* **4**(5), 2955–2963 (2010).
8. H. Wu, L. Hu, M. W. Rowell, D. Kong, J. J. Cha, J. R. McDonough, J. Zhu, Y. Yang, M. D. McGehee, and Y. Cui, "Electrospun metal nanofiber webs as high-performance transparent electrode," *Nano Lett.* **10**(10), 4242–4248 (2010).
9. L. Hu, H. Wu, and Y. Cui, "Metal nanogrids, nanowires, and nanofibers for transparent electrodes," *MRS Bull.* **36**(10), 760–765 (2011).
10. Y. Chen, Z. Ouyang, M. Gu, and W. Cheng, "Mechanically strong, optically transparent, giant metal superlattice nanomembranes from ultrathin gold nanowires," *Adv. Mater.* **25**(1), 80–85 (2013).
11. H. Guo, N. Lin, Y. Chen, Z. Wang, Q. Xie, T. Zheng, N. Gao, S. Li, J. Kang, D. Cai, and D.-L. Peng, "Copper nanowires as fully transparent conductive electrodes," *Sci. Rep.* **3**, 2323 (2013).
12. P.-C. Hsu, S. Wang, H. Wu, V. K. Narasimhan, D. Kong, H. Ryoung Lee, and Y. Cui, "Performance enhancement of metal nanowire transparent conducting electrodes by mesoscale metal wires," *Nat. Commun.* **4**, 2522 (2013).
13. H. Wu, D. Kong, Z. Ruan, P.-C. Hsu, S. Wang, Z. Yu, T. J. Carney, L. Hu, S. Fan, and Y. Cui, "A transparent electrode based on a metal nanotrough network," *Nat. Nanotechnol.* **8**(6), 421–425 (2013).

14. B. Han, K. Pei, Y. Huang, X. Zhang, Q. Rong, Q. Lin, Y. Guo, T. Sun, C. Guo, D. Carnahan, M. Giersig, Y. Wang, J. Gao, Z. Ren, and K. Kempa, "Uniform self-forming metallic network as a high-performance transparent conductive electrode," *Adv. Mater.* **26**(6), 873–877 (2014).
15. H.-G. Im, J. Jin, J.-H. Ko, J. Lee, J.-Y. Lee, and B.-S. Bae, "Flexible transparent conducting composite films using a monolithically embedded AgNW electrode with robust performance stability," *Nanoscale* **6**(2), 711–715 (2014).
16. M. G. Kang and L. J. Guo, "Nanoimprinted semitransparent metal electrodes and their application in organic light-emitting diodes," *Adv. Mater.* **19**(10), 1391–1396 (2007).
17. M. G. Kang, M. S. Kim, J. S. Kim, and L. J. Guo, "Organic solar cells using nanoimprinted transparent metal electrodes," *Adv. Mater.* **20**(23), 4408–4413 (2008).
18. D. S. Ghosh, T. L. Chen, and V. Pruneri, "High figure-of-merit ultrathin metal transparent electrodes incorporating a conductive grid," *Appl. Phys. Lett.* **96**(4), 041109 (2010).
19. M. G. Kang, T. Xu, H. J. Park, X. Luo, and L. J. Guo, "Efficiency enhancement of organic solar cells using transparent plasmonic Ag nanowire electrodes," *Adv. Mater.* **22**(39), 4378–4383 (2010).
20. P. B. Catrysse and S. Fan, "Nanopatterned metallic films for use as transparent conductive electrodes in optoelectronic devices," *Nano Lett.* **10**(8), 2944–2949 (2010).
21. P. Kuang, J.-M. Park, W. Leung, R. C. Mahadevaparam, K. S. Nalwa, T.-G. Kim, S. Chaudhary, K.-M. Ho, and K. Constant, "A new architecture for transparent electrodes: relieving the trade-off between electrical conductivity and optical transmittance," *Adv. Mater.* **23**(21), 2469–2473 (2011).
22. J. van de Groep, P. Spinelli, and A. Polman, "Transparent conducting silver nanowire networks," *Nano Lett.* **12**(6), 3138–3144 (2012).
23. K. Lee, S. H. Song, and J. Ahn, "FDTD simulation of transmittance characteristics of one-dimensional conducting electrodes," *Opt. Express* **22**(6), 6269–6275 (2014).
24. J. H. Park, D. Y. Lee, Y.-H. Kim, J. K. Kim, J. H. Lee, J. H. Park, T.-W. Lee, and J. H. Cho, "Flexible and transparent metallic grid electrodes prepared by evaporative assembly," *ACS Appl. Mater. Interfaces* **6**(15), 12380–12387 (2014).
25. H. J. Choi, S. Choo, P. H. Jung, J. H. Shin, Y. D. Kim, and H. Lee, "Uniformly embedded silver nanomesh as highly bendable transparent conducting electrode," *Nanotechnology* **26**(5), 055305 (2015).
26. J. van de Groep, D. Gupta, M. A. Verschuuren, M. M. Wienk, R. A. J. Janssen, and A. Polman, "Large-area soft-imprinted nanowire networks as light trapping transparent conductors," *Sci. Rep.* **5**, 11414 (2015).
27. H. M. Stec, R. J. Williams, T. S. Jones, and R. A. Hatton, "Ultrathin transparent Au electrodes for organic photovoltaics fabricated using a mixed mono-molecular nucleation layer," *Adv. Funct. Mater.* **21**(9), 1709–1716 (2011).
28. N. Tsutomu, T. Eishi, M. Kumi, F. Akira, and A. Koji, "Transparent aluminum nanomesh electrode fabricated by nanopatterning using self-assembled nanoparticles," *Appl. Phys. Express* **4**(2), 025201 (2011).
29. J. Zhu, X. Zhu, R. Hoekstra, L. Li, F. Xiu, M. Xue, B. Zeng, and K. L. Wang, "Metallic nanomesh electrodes with controllable optical properties for organic solar cells," *Appl. Phys. Lett.* **100**(14), 143109 (2012).
30. Q. G. Du, K. Sathiyamoorthy, L. P. Zhang, H. V. Demir, C. H. Kam, and X. W. Sun, "A two-dimensional nanopatterned thin metallic transparent conductor with high transparency from the ultraviolet to the infrared," *Appl. Phys. Lett.* **101**(18), 181112 (2012).
31. S. Y. Chou and W. Ding, "Ultrathin, high-efficiency, broad-band, omni-acceptance, organic solar cells enhanced by plasmonic cavity with subwavelength hole array," *Opt. Express* **21**(S1), A60–A76 (2013).
32. H. Y. Jang, S.-K. Lee, S. H. Cho, J.-H. Ahn, and S. Park, "Fabrication of metallic nanomesh: Pt nano-mesh as a proof of concept for stretchable and transparent electrodes," *Chem. Mater.* **25**(17), 3535–3538 (2013).
33. T. Gao, B. Wang, B. Ding, J. K. Lee, and P. W. Leu, "Uniform and ordered copper nanomeshes by microsphere lithography for transparent electrodes," *Nano Lett.* **14**(4), 2105–2110 (2014).
34. S.-M. Lee, J.-S. Chae, D.-Y. Kim, and K. C. Choi, "Plasmonic nanomeshes as large-area, low-resistive transparent electrodes and their application to ITO-free organic light-emitting diodes," *Org. Electron.* **15**(11), 3354–3361 (2014).
35. W. Wu and N. G. Tassi, "A broadband plasmonic enhanced transparent conductor," *Nanoscale* **6**(14), 7811–7816 (2014).
36. A. Hubarevich, M. Marus, A. Stsiapanau, A. Smirnov, J. Zhao, W. Fan, H. Wang, and X. Sun, "Transparent conductive nanoporous aluminium mesh prepared by electrochemical anodizing," *Phys. Status Solidi., A Appl. Mater. Sci.* **212**(10), 2174–2178 (2015).
37. M. Theuring, V. Steenhoff, S. Geissendörfer, M. Vehse, K. von Maydell, and C. Agert, "Laser perforated ultrathin metal films for transparent electrode applications," *Opt. Express* **23**(7), A254–A262 (2015).
38. Z. Wu, Z. Chen, X. Du, J. M. Logan, J. Sippel, M. Nikolou, K. Kamaras, J. R. Reynolds, D. B. Tanner, A. F. Hebard, and A. G. Rinzler, "Transparent, conductive carbon nanotube films," *Science* **305**(5688), 1273–1276 (2004).
39. D. Zhang, K. Ryu, X. Liu, E. Polikarpov, J. Ly, M. E. Tompson, and C. Zhou, "Transparent, conductive, and flexible carbon nanotube films and their application in organic light-emitting diodes," *Nano Lett.* **6**(9), 1880–1886 (2006).
40. D. S. Hecht, L. Hu, and G. Irvin, "Emerging transparent electrodes based on thin films of carbon nanotubes, graphene, and metallic nanostructures," *Adv. Mater.* **23**(13), 1482–1513 (2011).
41. Y. Zhu, Z. Sun, Z. Yan, Z. Jin, and J. M. Tour, "Rational design of hybrid graphene films for high-performance transparent electrodes," *ACS Nano* **5**(8), 6472–6479 (2011).
42. K. Ellmer, "Past achievements and future challenges in the development of optically transparent electrodes," *Nat. Photonics* **6**(12), 809–817 (2012).

43. I. Khrapach, F. Withers, T. H. Bointon, D. K. Polyushkin, W. L. Barnes, S. Russo, and M. F. Craciun, "Novel highly conductive and transparent graphene-based conductors," *Adv. Mater.* **24**(21), 2844–2849 (2012).
 44. G. Xu, J. Liu, Q. Wang, R. Hui, Z. Chen, V. A. Maroni, and J. Wu, "Plasmonic graphene transparent conductors," *Adv. Mater.* **24**(10), OP71–OP76 (2012).
 45. E. D. Palik, *Handbook of optical constants of solids* (Academic, Orlando, Fla., 1985), pp. 369–406.
 46. FDTD solutions; Lumerical Solutions, Inc.: B. C. Vancouver, Canada; www.lumerical.com.
 47. J. Braun, B. Gompf, G. Kobiela, and M. Dressel, "How holes can obscure the view: suppressed transmission through an ultrathin metal film by a subwavelength hole array," *Phys. Rev. Lett.* **103**(20), 203901 (2009).
-

1. Introduction

Transparent electrodes (TEs) are the essential components for optoelectronic devices such as light emitting diodes (LEDs) and solar cells. In recent decades, Indium doped tin oxide (ITO) thin films have been widely used as TEs in the optoelectronic devices. However, the cost of ITO is high due to the limited source of indium on Earth. Also, ITO film is brittle and not applicable for flexible devices [1]. Moreover, indium element easily penetrates to organic active layer and causes the performance degradation of the organic optoelectronic devices [2]. Due to the above mentioned drawbacks, alternative candidates such as ultrathin metal films [3, 4], random metal nanowires [5–15], metal grids [16–26], metal nanohole meshes [27–37], carbon nanotubes [38–40] and graphenes [41–44] have been studied extensively for realization of next-generation TE to replace current market dominating ITO TEs.

Nanostructured metal-based thin films have attracted much attention as one of the promising candidates for TEs. Harnessing the intrinsic high conductivity of metals that gives low sheet resistance, high transmittance can be achieved simultaneously by nano-structuring metal films. For example, transmittance as high as 90% and resistance as low as 2 Ω /sq have been simultaneously achieved by the random nanotrough gold network [13]. However, these types of random nanostructures are lack of uniformity and ordering. Instead, uniform and ordered metal nanogrids have also been proposed and studied extensively. It is reported in [22], transmittance of 91% and resistance of 6.5 Ω /sq have been achieved.

On the other hand, metal thin films with ordered subwavelength hole arrays also have been studied intensively due to the possibility of low cost and large area fabrication. It is reported in [33], thin copper film with order nanohole arrays has achieved a transmittance of ~80% and sheet resistance of ~17 Ω /sq. In [37], laser perforated ultrathin Ag film has been fabricated with transmittance of ~80% and sheet resistance of 54.6 Ω /sq. However, the transmittance and sheet resistance are still not comparable to those of ITO's. It is predicted theoretically that the aluminum (Al) nanohole meshes should have better optical and electrical performances than other studied metals such as silver, gold, copper and nickel [30]. Yet, the recent experimentally reported optical transmission is still less than 50% which is far lower than the requirement for TEs [28]. In this paper, we study the optical properties of Al ultrathin film with hexagonal nanohole arrays. Both experiments and simulations are performed for different nanohole arrays. Broadband enhanced transmission with transmittance over 60% from 430 nm to 750 nm is attained experimentally for the Al ultrathin film with hexagonal nanohole arrays. The underlying physics for such enhancement is also studied in detail.

2. Experimental methods

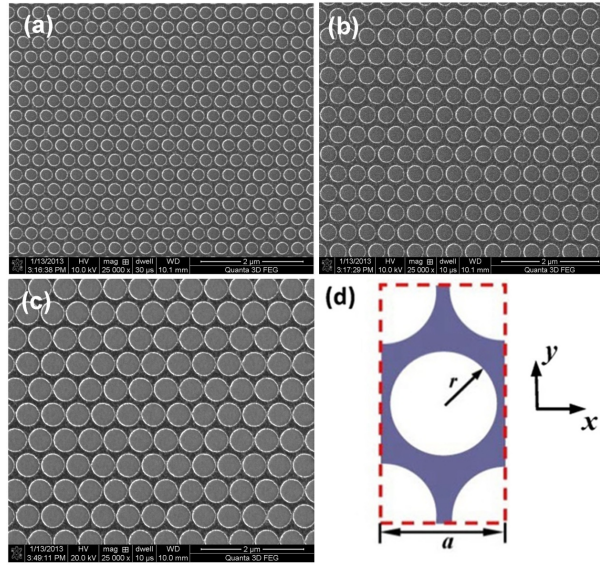


Fig. 1. SEM images of samples of aluminum ultrathin film with hexagonal nanohole arrays with (a) period $a = 300$ nm and radius $r = 127$ nm, (b) period $a = 400$ nm and radius $r = 163$ nm, (c) period $a = 500$ nm and radius $r = 202$ nm. (d) indicates the simulation unit cell.

2.1. Al nanohole structure fabrication

Experimental Al ultrathin films with hexagonal nanohole arrays are fabricated via electron-beam (E-beam) lithography. The fabrication process is briefly described as follows: (1) quartz substrates were cleaned and sputtered with aluminum layer; (2) PMMA (950K) was spin-coated on the surface of the aluminum layer to a thickness of 90 nm; (3) exposure of nanohole arrays with e-beam writer (CRESTEC 9500C). The accelerating voltage of the electron beam was 50 kV and the beam current was 200 pA; (4) development of the exposed nanoholes with IPA-DI developer, a mixture of isopropyl alcohol (IPA) and deionized (DI) water in a volume ratio 7:3; (5) the developed samples were then put to an etcher (Oxford Plasma 100) for etching. In the etching process, the PMMA resist worked as mask. The developed patterns (holes) were etched through to get aluminum nanohole arrays; (6) after the etching, the residual PMMA resist was removed with acetone and then cleaned with oxygen plasma. Samples of three types of hexagonal nanohole arrays are fabricated as shown in Fig. 1(a)-1(c). The periodicity is indicated as a and the radius of the hole is shown as r respectively [Fig. 1(d)]. We define the inverse volume filling fraction f of the nanostructured Al ultrathin film in one period as $f = 2\pi r^2 / \sqrt{3}a^2$ (the area ratio of the void region and the whole unit cell area). This fraction is the theoretical value of transmittance over nano-films made of perfect electrical conductor, at the ray-optics limit when photons wavelength is much smaller than the hole size. It is however, also related to the sheet resistance $R_{sq} \approx f(\rho_{Al} / d)$, which is to be minimized for TE. For our film of $d = 20$ nm aluminum, which has resistivity of $\rho_{Al} = 2.65 \times 10^{-8} \Omega \cdot \text{m}$, we get $R_{sq} = 0.8612 \Omega/\text{sq}$ for inverse filling fraction of $f = 0.65$. Figure 1(a) shows a sample with period $a = 300$ nm and radius $r = 127$ nm, Fig. 1(b) shows a sample with period $a = 400$ nm and radius $r = 163$ nm, and Fig. 1(c) shows a sample with period $a = 500$ nm and radius $r = 202$ nm respectively. For all three samples, the film thickness is fixed at $d = 20$ nm. All parameters indicated here are average values due to variations of the fabrication process.

2.2. Numerical simulation method

Simulations are performed in one unit cell of the periodic hexagonal nanohole arrays as shown in Fig. 1(d). In order to compare with the experimental measurements, a substrate of glass with refractive index of 1.5 is included in the simulations and considered as semi-infinite. The refractive index of Al is taken from [45]. The top of the nanostructured Al ultrathin film and the nanohole regions are air. The numerical calculations including the spectra and electric field (E-field) intensity distributions are performed with a full three dimensional finite-difference time-domain (FDTD) method within one unit cell [46]. In numerical simulations, the hole arrays are arranged in x - y plane [Fig. 1(d)] and a plane wave light is normally incident from the top of the structure. Here, we only consider the light with polarization in x direction by considering the symmetry of the hexagonal nanohole arrays [35]. In order to fully capture the plasmonic properties, a fine mesh is used in the numerical calculations with 3 nm mesh step in x and y directions and 1 nm mesh step in z direction. The amplitude of the transmitted and reflected light is recorded by a monitor placed in the substrate after the nanostructured Al ultrathin film and a monitor placed before the light source, which are then transformed to frequency domain and normalized to the source power. Correspondingly, we obtain the transmission ($T(\omega)$) and reflection ($R(\omega)$) coefficients. The absorption coefficient $A(\omega)$ is then determined by

$$A(\omega) = 1 - R(\omega) - T(\omega), \quad (1)$$

3. Results and discussion

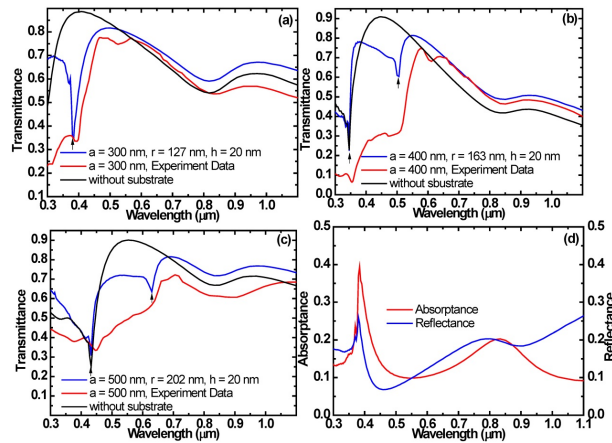


Fig. 2. Measured and simulated transmission spectra of the three fabricated samples (a) period $a = 300$ nm and radius $r = 127$ nm, (b) period $a = 400$ nm and radius $r = 163$ nm, (c) period $a = 500$ nm and radius $r = 202$ nm, the thickness of all three samples are fixed at $h = 20$ nm. Black lines show the simulated transmission spectra of all three samples without substrates, (d) Corresponding simulated absorption and reflection spectra of sample with period $a = 300$ nm, radius $r = 127$ nm and $h = 20$ nm.

The measured (red) and simulated (blue) transmission spectra of the three samples in Fig. 1(a)-1(c) are shown in Fig. 2(a)-2(c) correspondingly. The corresponding simulated absorption and reflection spectra of sample in Fig. 1(a) are shown in Fig. 2(d). The simulated spectra of the three samples without substrates are also presented as references (black). From Fig. 2(a) where the period $a = 300$ nm and $r = 127$ nm with filling fraction $f = 65\%$, it is confirmed that the transmittance is enhanced ($> 65\%$) in a broad wavelength range from 438 nm to 700 nm compared to the direct transmission through the hole arrays. For high transmittance $> 60\%$, the broad band wavelength range is from 430 nm to 750 nm. The measured transmittance agrees well with the simulation result for the long wavelength range down to the onset of the first-order diffraction at the glass substrate ($n_{\text{glass}} = 1.5$) region at

$\lambda = 450 \text{ nm}$ ($= n_{\text{glass}} a$). The reason of the deviation at short wavelength range between the simulated and measured spectra may be because that the measurement fails to capture the off-normal diffracted waves at the substrate region despite having transmitted through the Al film and the waveguided mode excited in the substrate [26]. Additionally, there is a transmission dip around $\lambda = 350 \text{ nm}$ for both experimental and simulated transmission spectra, as indicated by a black arrow in Fig. 2(a) while no such transmission dip around $\lambda = 350 \text{ nm}$ appears at the transmission spectrum of the suspended Al film without substrate. The transmission dip here is associated with the enhanced absorption and reflection as shown in Fig. 2(d). For the cases in Fig. 2(b) and Fig. 2(c), where the periodicities are $a = 400 \text{ nm}$ or $a = 500 \text{ nm}$, respectively, with similar inverse filling fraction f around 60%. According to the simulation results, both samples show broad transmission spectra for wavelengths from 400 nm to 700 nm, however, the measured transmission spectra for both cases are much narrower than the simulated results, and such discrepancy is again more pronounced at the short wavelength range below the onset of first order diffraction $\lambda < n_{\text{glass}} a$. It is also worth to note that different from the transmission spectrum in Fig. 2(a) where only one transmission dip is shown, in Figs. 2(b) and 2(c), there are two different transmission dips in each transmission spectrum (indicated by the black arrows in both figures). It is well known that periodic structures enable the light to couple to surface plasmon polaritons (SPPs). The SPP with wave vector \vec{k}_{spp} can be excited, when the incident light of wave vector \vec{k} and the reciprocal vector \vec{G} of the periodic structure satisfy the momentum-matching condition,

$$\vec{k}_{\text{spp}} = \vec{k}_{\square} + \vec{G}, \quad (2)$$

where \vec{k}_{\square} is the component of \vec{k} parallel to the film surface. For normal incidence and hexagonal arrays as we studied here, $\vec{k}_{\square} = 0$, the above equation becomes

$$k_{\text{spp}} = G, \quad (3)$$

and G is given by

$$G = \frac{4\pi}{a\sqrt{3}} \sqrt{i^2 + j^2 + ij}, \quad (4)$$

where i and j are integers. For ultrathin metal film, the SPPs excited at both Al surfaces couple with each other, and the dispersion relation for the optically thin film with thickness d can be derived for these coupled modes:

$$\tan h(\alpha_m d) = -\frac{\epsilon_m \alpha_m (\epsilon_{d1} \alpha_{d2} + \epsilon_{d2} \alpha_{d1})}{\epsilon_{d1} \epsilon_{d2} \alpha_m^2 + \epsilon_m^2 \alpha_{d1} \alpha_{d2}}, \quad (5)$$

Here, $\alpha_{d1}^2 = k_{\text{spp}}^2 - \epsilon_{d1} k_0^2$, $\alpha_m^2 = k_{\text{spp}}^2 - \epsilon_m k_0^2$, and $\alpha_{d2}^2 = k_{\text{spp}}^2 - \epsilon_{d2} k_0^2$, with k_0 being the incident light wave number. We consider asymmetric Al film structure with air on top and glass substrate underneath, where the dielectric constants of both materials are $\epsilon_{d1} = 1$ and $\epsilon_{d2} = 2.25$ respectively. The Al film thickness d is $d = 20 \text{ nm}$ which is on the order of the skin depth at the relevant wavelength range. We consider only excitation of the lowest-order SPP modes that lie within the relevant wavelength range, where the modes $(i, j) = \pm(1, 0)$, $\pm(0, 1)$ or $\pm(1, -1)$ in Eq. (4) are all degenerate. Such degeneracy gives rise to polarization independence at normal incidence, where different polarizations of incidence waves excites different superposition of these modes. While for thick films, the asymmetric upper and lower interfaces would each support an isolated SPP of distinct frequencies, for our ultrathin film structure, the SPPs at the two interfaces weakly couple to form a pair of orthogonal

hybridized eigenmodes, with their distinct resonance wavelengths resolved by Eq. (5). For periodic arrays with $a = 300$ nm, the calculated SPP wavelengths are at around $\lambda = 258$ nm and $\lambda = 384$ nm. For periodic arrays with $a = 400$ nm, the calculated SPP wavelengths are at around $\lambda = 346$ nm and $\lambda = 515$ nm. For periodic arrays with $a = 500$ nm, the calculated SPP wavelengths are at around $\lambda = 427$ nm and $\lambda = 647$ nm. The calculated SPP resonance wavelengths are all coincide with the corresponding transmission dips in the spectra in Fig. 2(a)-2(c) though for the $a = 300$ nm structure, the SPP peak at $\lambda = 258$ nm is substantially outside the visible spectrum and the relevant wavelength range of TEs, and are excluded from our simulation and measurement that we show in Fig. 2(a). We further compare the results with the simulated spectra of the corresponding nanostructured Al film without substrate (symmetric structures), the transmission dips at $\lambda = 346$ nm for $a = 400$ nm, and $\lambda = 427$ nm for $a = 500$ nm structures roughly coincide for both the symmetric and asymmetric cases, as shown in Figs. 2(b) and 2(c) respectively. These results confirm that among the pair of the transmission dips, the short-wavelength dips ($\lambda = 346$ nm for $a = 400$ nm structure in Fig. 2(b) and $\lambda = 427$ nm for $a = 500$ nm structure in Fig. 2(c)) correspond to the hybridized SPPs dominantly excited at air-Al interface, while the long-wavelength dips ($\lambda = 515$ nm for $a = 400$ nm structure in Fig. 2(b) and $\lambda = 647$ nm for $a = 500$ nm structure in Fig. 2(c)) correspond to the hybridized dips dominantly excited at the glass-Al interface. The SPP resonances can interfere with the direct-path transmission through the hole region and form Fano-type resonances [35, 47]. We believe that the transmission dips are owing to the strong absorption at the SPP resonance, when the momentum-matching condition in Eq. (2) satisfies. Also, strong destructive interference of the excited SPPs and the directly transmitted light leads to strong reflection from the top surface as shown in Fig. 2(d). Meanwhile, the constructive interference of the excited SPPs and the directly transmitted light contributes to the broadband transmission enhancement for wavelength range larger than the SPP resonance wavelength.

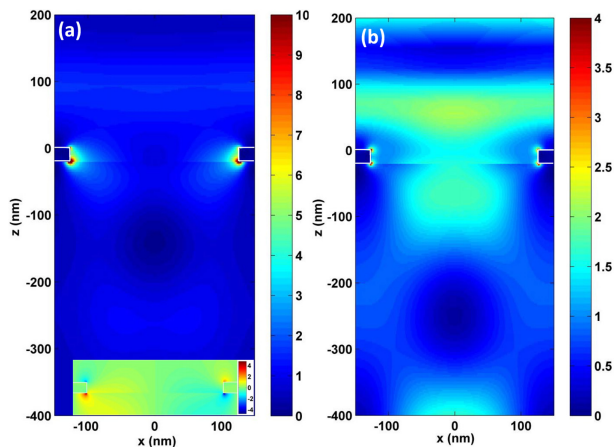


Fig. 3. E-field intensity distributions within x - z plane at center of y direction ($y = 0$) of a) $\lambda = 384$ nm, and b) $\lambda = 480$ nm for Al ultrathin film with hexagonal nanohole arrays with $a = 300$ nm, $r = 127$ nm and $h = 20$ nm. Inset of (a) shows the E_z component of the E-field distribution.

The excitation of the SPPs can further be confirmed by the E-field intensity distributions in Fig. 3 at two different wavelengths of $\lambda = 384$ nm and $\lambda = 480$ nm respectively for the nanostructured Al film with period $a = 300$ nm, radius $r = 127$ nm and thickness $d = 20$ nm on glass substrate. The E-field intensity distributions are obtained in x - z plane at the centre of y direction ($y = 0$), Al-dielectric interfaces are indicated with white lines. $\lambda = 384$ nm corresponds to the wavelength where the transmission dip reaches minimum and $\lambda = 480$ nm corresponds to the wavelength where the broadband high transmission reaches the maximum. Figure 3(a) shows the E-field intensity distribution at $\lambda = 384$ nm, it is clear that there are

strong E-field localization at the interface of Al and the substrate which confirms the excitation of the SPP. The excited SPP resonance enhances absorption in the Al film and introduces an additional transmission path that interfere destructively with the directly transmitted light at the substrate region, enhancing reflection at the top surface of Al film [Fig. 2(d)], which attribute to the transmission dip as shown in Fig. 2(a). Inset of Fig. 3(a) shows the E_z component of the E-field, it clearly demonstrates that the resonant mode is an antisymmetric bonding mode. From E-field intensity distribution in Fig. 3(b), the E-field intensity is reduced compared to that in Fig. 3(a). Accordingly, most of the light is transmitted through the optical mode sustained by the nanohole, with constructive interference between the SPP and the directly transmitted light. These are typical characteristics of Fano resonances [35].

From the view of TEs, the SPPs excitation is an undesirable feature if it appears within the interested wavelength range because the excitation of SPPs will introduce enhanced absorption and reflection which will cause transmission dips in the transmission spectrum. It is better to tune the excitation wavelength of SPP out of the interested wavelength range by using smaller nanohole array period. To evaluate the transmission performance of the nanostructured Al film as TEs, the average transmission from 400 nm to 1000 nm weighted for the AM 1.5 spectrum is calculated. The calculated average transmission is 0.7186, 0.6565 and 0.7098 for the structures with period $a = 300$ nm and radius $r = 127$, period $a = 400$ nm and radius $r = 163$ and period $a = 500$ nm and radius $r = 202$ nm respectively. In this work, nanostructured Al film with period $a = 300$ nm and radius $r = 127$ nm is more suitable for TEs. Apart from changing the lattice period, it is reported that if the ratio between hole radius r and period a is large ($r/a > 0.45$), the transmission dip will disappear and the enhanced broadband transmission background remains at the same wavelength [35]. Fig. 4 shows the transmission spectra of our nanohole ultrathin film for different hole radius r with fixed film thickness $d = 20$ nm and period $a = 500$ nm. With the increase of hole radius, the transmission dip at $\lambda = 647$ nm becomes weaker and start to disappear when the hole radius reaches $r = 220$ nm which agrees well with the conclusion in [35]. In the future, we will try to fabricate larger hole radius nanohole arrays and study both transmission and sheet resistance properties. If we can make the hole radius much larger with acceptable sheet resistance ($\sim 10 \Omega/\text{sq.}$, for example, for solar cell application), larger periods such as $a = 400$ nm and $a = 500$ nm are preferred for TEs with broad and high transmittance in both visible and infrared wavelength range.

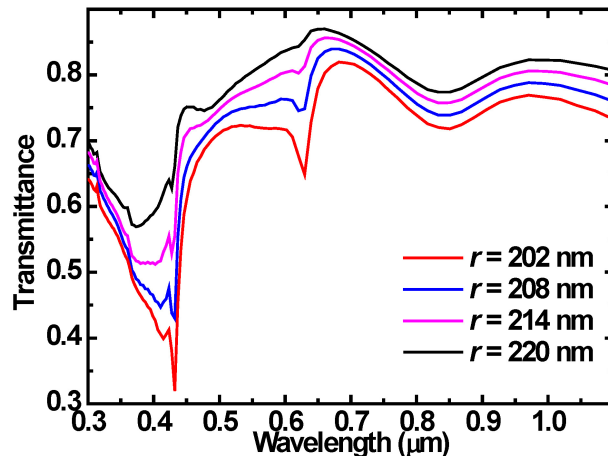


Fig. 4. Simulated transmission spectra of aluminum ultrathin films with hexagonal nanohole arrays of various hole radius with period $a = 500$ nm and thickness $h = 20$ nm.

4. Conclusions

In summary, we have fabricated aluminum ultrathin films with hexagonal nanohole arrays and measured the transmission spectra in the wavelength range from 300 nm to 1100 nm. For the period $a = 300$ nm, radius $r = 163$ nm and thickness $d = 20$ nm, the aluminum ultrathin film with hexagonal nanohole arrays shows broad and enhanced transmittance larger than 60% from 430 nm to 750 nm which surpasses the previously reported transmittance of the aluminum nanohole arrays [28]. According to our numerical analysis, the constructive Fano-type interference between the excited surface plasmon polaritons and the directly transmitted light contributes to the broadband enhanced transmittance. Meanwhile, there is a pair of transmission dips which is caused by both enhanced reflection from destructive Fano-type interference between the excited surface plasmon polaritons and the directly transmitted light, and enhanced absorption within the SPP resonance.